

Viscous effect on neutral radical spatial distribution in microwave plasma chemical vapor deposition

Zhiguo Tian, Bin Liu and Moran Wang* 

Department of Engineering Mechanics, Tsinghua University, Beijing 100084, People's Republic of China

E-mail: mrwang@tsinghua.edu.cn

Received 5 November 2024, revised 23 February 2025

Accepted for publication 5 March 2025

Published 13 March 2025



CrossMark

Abstract

Microwave plasma chemical vapor deposition (MPCVD) is one of the most promising methods for producing single-crystal diamond (SCD), which is acclaimed as the ‘ultimate semiconductor’ material. However, high-quality large-size SCD is still lacking. Previous research asserts the dominance of the electric field and ignores the influence of the flow. In the present work, an analysis of the orders of magnitude is conducted on the fluid description of the plasma to obtain simplified governing equations based on the typical working parameters of the MPCVD. Our theoretical derivation concludes that the spatial distribution of the neutral radical is determined not only by the density gradient but also by the viscous interaction with the neutral gas flow. For verification, the set of governing equations, encompassing Maxwell's equations, electron and neutral radical number density equations, and laminar Navier–Stokes equations, is numerically solved. The simulation results reveal that the non-uniformity of the spatial distribution of the neutral radical increases with the difference of the inlet velocity, corroborating our theoretical analyses. This finding provides a novel regulatory approach for producing high-quality large-size SCD and can possibly be extended to other CVD processes for controlling product quality.

Keywords: diamond, microwave plasma chemical vapor deposition, neutral radical, viscous effect, spatial distribution

1. Introduction

Single-crystal diamond (SCD) exhibits exceptional properties, boasting unparalleled thermal conductivity, hole mobility, and bandgap width when compared to single-crystal silicon, silicon carbide, gallium nitride, and gallium arsenide (Neves and Nazaré 2001). Consequently, it stands as a highly promising candidate for the semiconductor industry, and is well recognized as the ‘ultimate semiconductor’ material. However, the efficient manufacture of high-quality large-size SCD remains a formidable challenge. Presently, microwave plasma chemical

vapor deposition (MPCVD) (Kamo *et al* 1988) is emerging as the mainstream and most promising technique for depositing SCD compared with the high-temperature high-pressure method (Bundy *et al* 1955, Gong *et al* 2024).

In MPCVD, the microwave is directed into a resonant chamber, which contains H₂–CH₄ gas mixture with a pressure of about 10⁴ Pa, possibly adding Ar, N₂, O₂, or other minor components. The microwave is concentrated on the chamber and accelerates free electrons, leading to the excitation of the gas through collisions. This microwave-excited plasma is in non-equilibrium, characterized by electron temperatures typically around 10⁴ K (Narishige *et al* 2000, Hassouni *et al* 2010, Derkaoui *et al* 2014), significantly exceeding the ion and gas temperatures, which are typically around 10³ K (Gicquel *et al*

* Author to whom any correspondence should be addressed.

1994, Hassouni *et al* 1999a, 2010). Generally, the ionization degree is low, at about 10^{-6} (Gicquel *et al* 1994, Derkaoui *et al* 2014), and the electron number density is on the magnitude of 10^{17} m^{-3} (Grotjohn *et al* 2000, Narishige *et al* 2000, Hassouni *et al* 2010, Derkaoui *et al* 2014). The excited carbon-containing groups facilitate SCD growth, and the mechanism for deposition can possibly be phenomenally described by the Goodwin model (Goodwin 1993a, 1993b), in which the neutral radicals, including CH_3 and H , play a key role. To date, the largest SCD deposited by MPCVD is only about 4 inches (Schreck *et al* 2017). A deeper understanding of physics in MPCVD is imperative for further advancement of SCD.

Most preceding studies of MPCVD devices have predominantly relied on numerical simulations of plasmas using macroscopic models, which overlook the influence of fluid flow. The electric field stands as the foundational energy source for the entire system, obtainable through numerically solving Maxwell's equations, which is regarded as the determining factor in device optimization even in recent years (An *et al* 2015, Vikharev *et al* 2018). Subsequent fields, encompassing density, temperature, and flow, are intricately linked to the electromagnetic field (Hagelaar *et al* 2004). The gas pressure in MPCVD is about 10^4 Pa , which is beyond the capability of the particle-in-cell/Monte-Carlo method, prompting researchers to turn to the fluid description of plasma (Alves *et al* 2018). The pioneering endeavor in simulating MPCVD, in which the electromagnetic field and electron number density are simultaneously calculated in a simplified form, dates back about three decades to the work of F uner *et al* (1995, 1999). The authors assumed that the local electron number density is linearly related to the local electric magnitude. Even though the coupled mechanism is overly simplified, they successfully predicted the existence of a secondary plasma ball for 2D axis-symmetric simulation in stationary conditions, which has practical meaning for actual deposition. After this, the model was further developed by introducing gradient-driven diffusion (Pleuler *et al* 2002), which has been adopted by many following researchers (Li *et al* 2011, 2020, Su *et al* 2014, An *et al* 2015, Wang *et al* 2019, Zhai *et al* 2024) because of its easy implementation. However, this model is limited to providing information solely on the electric and electron number density fields. In further advancements, other researchers (Yamada *et al* 2007, 2011, 2015) incorporated the Arrhenius law and the Ohmic law into the original model and, in this way, the density field for other ions, atoms, molecules, and active groups could be obtained along with the temperature field. Constrained by the detailed analysis ability of reactions and limited computing resources, they only consider limited types of reactions and fit them by effective parameters to save the effort of solving any energy equations. Careful and thorough study of the reactions for $\text{H}_2\text{-CH}_4$ mixture in MPCVD was implemented using the collisional-radiation model by Hassouni *et al* (1999a, 1999b, 2010) with a different numerical framework. They distinguished transitional, rotational, and vibrational modes of polyatomic molecules, respectively, and solved three additional energy equations for pure H_2 in 2D axis-symmetric

simulations (Hassouni *et al* 1999a) and for $\text{H}_2\text{-CH}_4$ mixture in the 1D case (Hassouni *et al* 2010) without fluid flow. It should be noted that they further developed their model to discuss the buoyancy effect on the formation of a secondary plasma ball in the 2D axis-symmetric case (Prasanna *et al* 2016, 2017), in which the reactor was assumed to have no inlets or outlets. Other strategies have been developed in the past decade, including simulating the plasma ball and neighboring region rather than the whole chamber in the 2D case to reduce the simulation cost (Mankelevich *et al* 2008, Ashfold and Mankelevich 2022, 2023), and assuming the plasma ball to be a uniform heat source in the 3D case using commercial software to spare the effort of calculating chemical reactions (Mesbahi *et al* 2013).

Physically speaking, electrons have high velocity and minimal mass, rendering them unaffected, while the ion and neutral radical velocity is comparable with that of the neutral gas and would be significantly influenced by the neutral gas flow. This is intuitively straightforward, but the underlying mechanism is currently not clear. Some recent experiments reveal that the asymmetric gas inlet velocity (Wang *et al* 2020) and different gas inlet arrangements (Teng *et al* 2023, Zhao *et al* 2023) can cause 3D non-uniformity of the spatial distribution of ion and neutral radicals and even accelerate the deposition rate in MPCVD. These experimental observations provide a potential regulatory method for actual production and need to be theoretically explained for better usage. To uncover the physical mechanism it is necessary to respectively describe ions and neutral gas flow, and to properly propose their coupling mechanism.

2. Physical and mathematical models

The Boltzmann equation is a kinetic and statistical description of the weakly-ionized plasma (Kremer 2010, Alves *et al* 2018), which provides a parallel approach for treating electrons, ions, and molecules. Adopting the two-term approximation method, the electron transport properties and rate coefficients can be theoretically calculated (Hagelaar and Pitchford 2005). It is also possible to obtain the transport coefficients by the Chapman-Enskog method (Boulos *et al* 2023). Despite these achievements, it is technically impossible to solve the Boltzmann equation in 3D space, and therefore the fluid description of plasma by finding the momentum for the Boltzmann equation is adopted for studying the spatial distribution of plasma at high pressure. Physically speaking, the Boltzmann equation is more fundamental and we resort to it to uncover the unknown mechanism of flow influence on plasma spatial distribution.

2.1. Fluid descriptions of plasma

The starting point is the Boltzmann equation, which is a complex differential-integral equation that describes the evolution of different particles. By integrating the Boltzmann equation in

Table 1. Typical substances in the H₂–CH₄ mixture plasma used in MPCVD.

Particle type	Magnitude of number density	Typical chemical substances	Subscript	Comment
Electron	$\sim 10^{17} \text{ m}^{-3}$	e	e	Experimental value range from (Derkaoui <i>et al</i> 2014, Narishige <i>et al</i> 2000, Grotjohn <i>et al</i> 2000). Affected by microwave power and gas pressure.
Ion	$\sim 10^{17} \text{ m}^{-3}$	$\text{H}^+, \text{H}^-, \text{H}_2^+, \text{H}_3^+, \text{CH}_4^+$	i	Assumed to be the same as n_e .
Neutral radical	$\sim 10^{20} \text{ m}^{-3}$	H, H^*	n	Value taken from (Hassouni <i>et al</i> 1999b, 2010) when electron energy is 1 eV and total gas density is 10^{24} m^{-3} .
Gas mixture	$\sim 10^{24} \text{ m}^{-3}$	H_2, CH_4	g	Total gas density is 10^{24} m^{-3} , for the gas pressure of 10^4 Pa .

velocity space (Bhatnagar *et al* 1954, Kremer 2010, Loureiro and Amorim 2016, Alves *et al* 2018), the zeroth momentum for the Boltzmann equation is the continuity equation and the first momentum is the momentum equation:

$$\frac{\partial n_\alpha}{\partial t} + \frac{\partial (n_\alpha u_{\alpha k})}{\partial x_k} = S_\alpha, \quad (1)$$

$$m_\alpha \frac{\partial (n_\alpha u_{\alpha k})}{\partial t} + n_\alpha m_\alpha u_{\alpha j} \frac{\partial u_{\alpha k}}{\partial x_j} + \frac{\partial p_{jk}}{\partial x_j} - en_\alpha E_k = -m_\alpha n_\alpha u_{\alpha k} \nu_\alpha, \quad (2)$$

where the particle $\alpha \in \{e, i, n, g\}$ for electron, ion, neutral radical, and gas mixture, respectively, m_α is the particle mass, n_α is the particle number density, $u_{\alpha k}$ is the particle mean velocity in direction k , S_α is the source term, which includes the generation and loss of the particle α , E_k is the electric field magnitude, and ν_α is the collision frequency. p_{jk} is the pressure tensor and can be expressed as $p_{jk} = p\delta_{ij} + p_{\langle ij \rangle}$, in which δ_{ij} is the Kronecker delta function and $p_{\langle ij \rangle}$ is the off-diagonal component of the pressure tensor, which demonstrates the viscous effect. The Lorentz force is expressed as eE_k for electrons and ions, where E_k is the electric field magnitude, in which we only consider ions with unit charge for simplicity. The typical substances in the H₂–CH₄ mixture plasma used in MPCVD are demonstrated in table 1. The ionization degree is low, generally smaller than 10^{-6} (Gicquel *et al* 1994, Derkaoui *et al* 2014), and the neutral radicals are denser than the electrons and ions since there are additional thermal chemical reactions for neutral radical production. Therefore, physically, the gas mixture can be regarded as a background gas whose number density remains constant, where the electrons, ions, and neutral radicals are dilute.

For MPCVD, the electron, ion, neutral radical, and gas mixture are in non-equilibrium, where the electron velocity is much higher than that of the others. This indicates that the viscous force exerted on the electron, which is the off-diagonal part of the pressure tensor p_{jk} , can be omitted, as prior researchers did (Hassouni *et al* 2010, Prasanna *et al* 2016). The

ion velocity is of a comparable magnitude to that of neutral gas, but the ion is accompanied by a direct current component to maintain the quasi-neutrality of the plasma. In microwave discharge, this can be imposed by the ambipolar diffusion, and the ion is mainly influenced by the electron. However, the neutral radical is barely affected by the electric field since it has no charge. Consequently, the viscous force is retained for neutral radicals and omitted for electrons and ions in our study:

$$\frac{\partial p_{jk}}{\partial x_j} = \begin{cases} k_b T_e \frac{\partial n_e}{\partial x_k}, & \text{for electron} \\ k_b T_i \frac{\partial n_i}{\partial x_k}, & \text{for ion} \\ k_b T_n \frac{\partial n_n}{\partial x_k} + \mu_n \frac{\partial^2 u_n}{\partial x_j \partial x_j}, & \text{for neutral radical} \end{cases}, \quad (3)$$

where T_e, T_i, T_n are the electron, ion, and neutral radical temperature, and k_b is the Boltzmann constant. Shortly speaking, equation (3) is our key contribution and demonstrates that in our present work, the electrons and ions are treated as inviscid fluids, while the neutral radical is regarded as a viscid fluid. The following part will show how this can lead to an influencing effect.

In summary, the momentum equations for the electron, ion, and neutral radical are

$$m_e \frac{\partial (n_e u_{ek})}{\partial t} + n_e m_e u_{ej} \frac{\partial u_{ek}}{\partial x_j} + k_b T_e \frac{\partial n_e}{\partial x_k} + n_e m_e \nu_e u_{ek} + en_e E_k = 0, \quad (4)$$

$$m_i \frac{\partial (n_i u_{ik})}{\partial t} + n_i m_i u_{ij} \frac{\partial u_{ik}}{\partial x_j} + k_b T_i \frac{\partial n_i}{\partial x_k} + n_i m_i \nu_i u_{ik} + en_i E_k = 0, \quad (5)$$

$$m_n \frac{\partial (n_n u_{nk})}{\partial t} + n_n m_n u_{nj} \frac{\partial u_{nk}}{\partial x_j} + k_b T_n \frac{\partial n_n}{\partial x_k} + \mu_n \frac{\partial^2 u_{nk}}{\partial x_j \partial x_j} + n_n m_n \nu_n u_{nk} = 0. \quad (6)$$

The gas mixture is hardly influenced by other dilute substances because of the very low ionization degree, and can

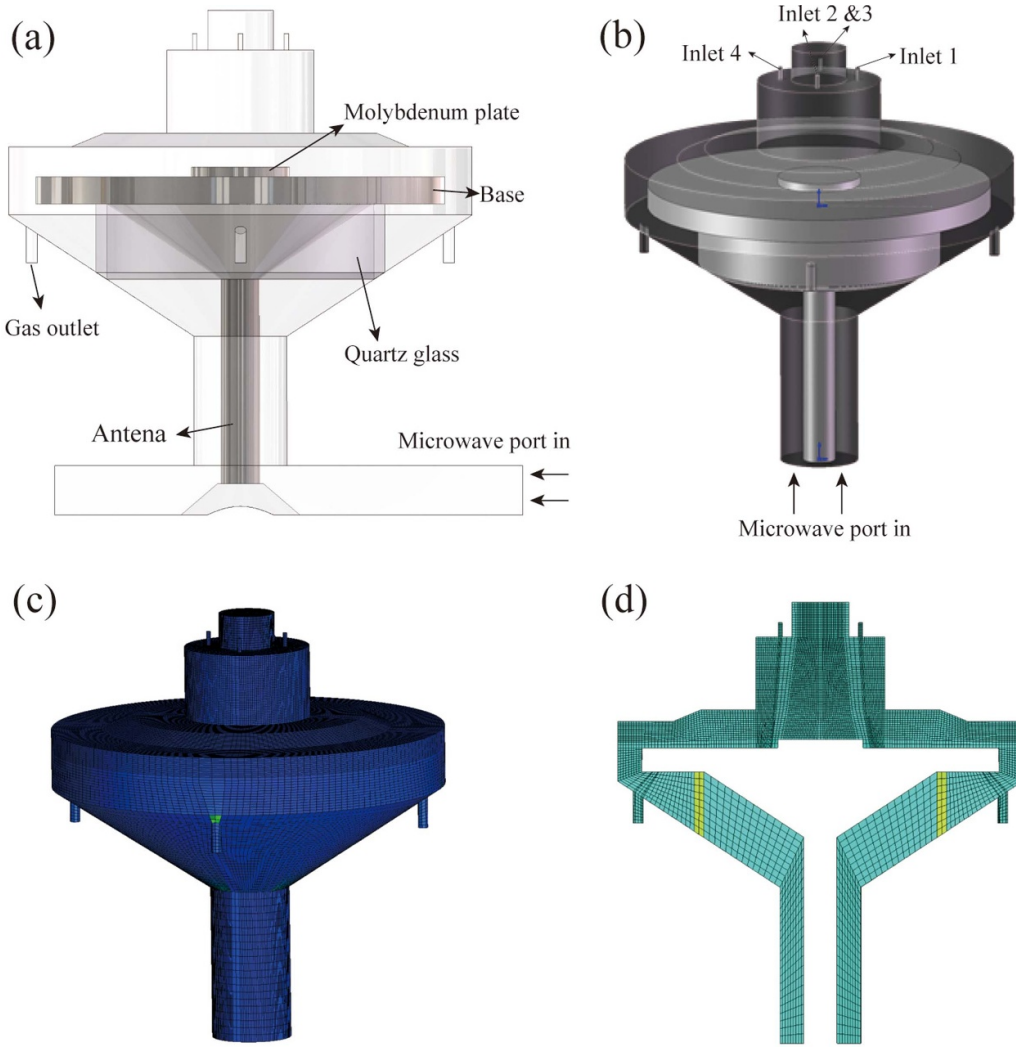


Figure 1. The 3D geometry of the MPCVD chamber in the present study and corresponding mesh. (a) 3D geometry. The quartz glass separates the upper and lower side, which can be transmitted by microwave and cannot pass gas. (b) The simulated domains. (c) Structured grids in 3D form. (d) A sectional drawing of the mesh.

therefore be fully described by the steady-state incompressible Navier–Stokes equations:

$$\frac{\partial u_{gk}}{\partial t} + \frac{\partial u_{gk}}{\partial x_k} = 0, \quad (7)$$

$$\rho_g \frac{\partial u_{gk}}{\partial t} + \rho_g u_{gj} \frac{\partial u_{gk}}{\partial x_j} = -\frac{\partial p}{\partial x_k} + \mu_g \frac{\partial^2 u_{gk}}{\partial x_j \partial x_j}. \quad (8)$$

The constants are $k_b = 1.38 \times 10^{-23} \text{JK}^{-1}$, $m_e = 0.91 \times 10^{-30} \text{kg}$, and $e = 1.60 \times 10^{-19} \text{C}$. We briefly summarize the assumptions we are currently adopting and will use in the following parts:

(a) The temperature distribution is assumed to be spatially constant. This is because the gas mixture inlet velocity that we consider is small, and can hardly influence the temperature distribution. Therefore, the temperature distribution

should always be axis-symmetric for our considered axis-symmetric chamber in figure 1, which barely has a chance to cause any asymmetric result. Based on this, we assume the temperature to be spatially constant, to save us time solving the temperature equation. Moreover, this assumption can guarantee us to adopt the incompressible Navier–Stokes equations for the gas mixture, which can also save the computational cost;

- (b) We focus on microwave discharge operating at a high gas pressure, at a magnitude of 0.1 atmospheric pressure. Volumetric generation and recombination are dominant mechanisms. Hence, we assume that the generation is proportional to the electric field energy and that the recombination is related to the number density.
- (c) We do not consider specific chemical reactions in our present work due to their time-consuming calculation. We assume that the mixture is composed of electrons, ions, neutral radicals, and original neutral gas, but cannot tell each component apart.

This set of equations is too complex to directly solve. Fortunately, they can be simplified by considering the different magnitudes of each term. In the next subsection, we conduct an analysis of the order of magnitude on each term of equations (1), (4)–(6) to simplify them.

2.2. Analysis of order of magnitude

The analysis of the order of magnitude is a powerful tool for simplifying complex governing equations based on a physical understanding of the specific process, which is generally adopted for analyzing the Navier–Stokes equations in fluid mechanics. In the present work, the fluid description of the plasma and its equation set, including equations (1), (4)–(6), is too complex to be fully solved numerically. Therefore, the analysis of the order of magnitude is conducted to simplify them. First, we nondimensionalize equations (4)–(6) by choosing

$$\begin{aligned} \tilde{n}_e &= \frac{n_e}{n_{e0}}, \tilde{u}_{ek} = \frac{u_{ek}}{u_{e0}}, \tilde{T}_e = \frac{T_e}{T_{e0}}, \tilde{x}_j = \frac{x_j}{L}, \tilde{t} = \frac{t}{t_0} \\ \tilde{n}_i &= \frac{n_i}{n_{i0}}, \tilde{u}_{ik} = \frac{u_{ik}}{u_{i0}}, \tilde{T}_i = \frac{T_i}{T_{i0}}, \tilde{E}_k = \frac{E_k}{E_{k0}} \\ \tilde{n}_n &= \frac{n_n}{n_{n0}}, \tilde{u}_{nk} = \frac{u_{nk}}{u_{n0}}, \tilde{T}_n = \frac{T_n}{T_{n0}}, \end{aligned} \quad (9)$$

where parameters with the tilde above are nondimensionalized. Parameters with the subscript 0 are the characteristic quantities, whose magnitudes are estimated as the maximum values of the corresponding parameters by the general conditions in MPCVD and listed in table 2.

The nondimensionalized form of equation (4) by dividing $n_{e0}m_e\nu_{e0}u_{e0}$ is

$$\begin{aligned} \frac{1}{t_0\nu_e} \frac{\partial(\tilde{n}_e\tilde{u}_{ek})}{\partial\tilde{t}} + \frac{u_{e0}}{\nu_{e0}L} \tilde{n}_e\tilde{u}_{ej} \frac{\partial\tilde{u}_{ek}}{\partial\tilde{x}_j} + \frac{k_bT_{e0}}{m_e\nu_{e0}u_{e0}L} \tilde{T}_e \frac{\partial\tilde{n}_e}{\partial\tilde{x}_k} \\ + \tilde{n}_e\tilde{u}_{ek} + \frac{eE_{k0}}{m_eu_{e0}\nu_{e0}} \tilde{n}_e\tilde{E}_k = 0. \end{aligned} \quad (10)$$

The magnitudes of each term are $\mathcal{O}(\frac{1}{t_0\nu_e}) \sim \mathcal{O}(1)$, $\mathcal{O}(\frac{u_{e0}}{\nu_eL}) \sim \mathcal{O}(10^{-3})$, $\mathcal{O}(\frac{k_bT_{e0}}{m_e\nu_eu_{e0}L}) \sim \mathcal{O}(10^{-3})$, and $\mathcal{O}(\frac{eE_{k0}}{m_eu_{e0}\nu_e}) \sim \mathcal{O}(1)$, respectively, by taking the magnitudes in table 2. Based on these orders of magnitude, equation (10) can be separated as

$$\mathcal{O}(1) : \frac{\partial(\tilde{n}_e\tilde{u}_{ek})}{\partial\tilde{t}} + \tilde{n}_e\tilde{u}_{ek} + \tilde{n}_e\tilde{E}_k = 0, \quad (11)$$

$$\mathcal{O}(\epsilon_e) : \tilde{n}_e\tilde{u}_{ej} \frac{\partial\tilde{u}_{ek}}{\partial\tilde{x}_j} + \tilde{T}_e \frac{\partial\tilde{n}_e}{\partial\tilde{x}_k} = 0, \quad (12)$$

where $\epsilon_e \ll 1$ is a small amount that is estimated to be 10^{-3} . The dimensional form of equation (11) is $m_e \frac{\partial(n_e u_{ek})}{\partial t} + n_e m_e \nu_e u_{ek} + en_e E_k = 0$, which is the local momentum equation for electrons and has the same form as in Hassouni et al (1999b, 2010). In the steady state, without the time dependence, equation (11) means that the microwave energy is transferred to electrons by high-frequency collisions, which

are characterized by the collision frequency ν_e and are a very fast process. Equation (12) describes the diffusion process, driven by the density gradient, and this is a much slower process.

Similarly, for convenient comparison of orders of magnitude with equation (10), nondimensionalizing equation (5) by dividing $n_{e0}m_e\nu_{e0}u_{e0}$ obtains

$$\begin{aligned} \frac{n_{i0}m_i\nu_{i0}u_{i0}}{n_{e0}m_e\nu_{e0}u_{e0}} \left(\frac{1}{t_0\nu_i} \frac{\partial(\tilde{n}_i\tilde{u}_{ik})}{\partial\tilde{t}} + \frac{u_{i0}}{\nu_iL} \tilde{n}_i\tilde{u}_{ij} \frac{\partial\tilde{u}_{ik}}{\partial\tilde{x}_j} + \frac{k_bT_{i0}}{m_i\nu_iu_{i0}L} \tilde{T}_i \frac{\partial\tilde{n}_i}{\partial\tilde{x}_k} \right. \\ \left. + \tilde{n}_i\tilde{u}_{ik} + \frac{eE_{k0}}{m_iu_{i0}\nu_i} \tilde{n}_i\tilde{E}_k \right) = 0, \end{aligned} \quad (13)$$

where $\mathcal{O}(\frac{1}{t_0\nu_i}) \sim \mathcal{O}(1)$, $\mathcal{O}(\frac{u_{i0}}{\nu_iL}) \sim \mathcal{O}(10^{-9})$, $\mathcal{O}(\frac{k_bT_{i0}}{m_i\nu_iu_{i0}L}) \sim \mathcal{O}(1)$, $\mathcal{O}(\frac{\mu_i}{n_{i0}m_i\nu_iL^2}) \sim \mathcal{O}(1)$ and $\mathcal{O}(\frac{eE_{k0}}{m_iu_{i0}\nu_i}) \sim \mathcal{O}(10^3)$, respectively. The term $\frac{eE_{k0}}{m_iu_{i0}\nu_i} \tilde{n}_i\tilde{E}_k$ in equation (13) corresponds to the electric force exerted upon the ion, and its magnitude is much larger than others. This induces discharge separation, but the electron balances it to maintain the quasi-neutrality of the plasma, which will be properly modeled as ambipolar diffusion in the following parts. The other term is the convective term, $\frac{u_{i0}}{\nu_iL} \tilde{n}_i\tilde{u}_{ij} \frac{\partial\tilde{u}_{ik}}{\partial\tilde{x}_j}$, which is so small that it can be omitted since the ion velocity is very low. Therefore, these two terms are disregarded from equation (13). Since $\mathcal{O}(\frac{n_{i0}m_i\nu_{i0}u_{i0}}{n_{e0}m_e\nu_{e0}u_{e0}}) \sim \mathcal{O}(10^{-3}) \sim \mathcal{O}(\epsilon_e)$, we can acquire

$$\mathcal{O}(\epsilon_e) : \frac{\partial(\tilde{n}_i\tilde{u}_{ik})}{\partial\tilde{t}} + \tilde{T}_i \frac{\partial\tilde{n}_i}{\partial\tilde{x}_k} + \tilde{n}_i\tilde{u}_{ik} = 0. \quad (14)$$

For the steady state, equation (14) means the driving force for ions is the density gradient $\tilde{T}_i \frac{\partial\tilde{n}_i}{\partial\tilde{x}_k}$, which is balanced by the collision term $\tilde{n}_i\tilde{u}_{ik}$.

Following the same process, nondimensionalizing equation (6) by dividing $n_{e0}m_e\nu_{e0}u_{e0}$ obtains

$$\begin{aligned} \frac{n_{n0}m_n\nu_{n0}u_{n0}}{n_{e0}m_e\nu_{e0}u_{e0}} \left(\frac{1}{t_0\nu_n} \frac{\partial(\tilde{n}_n\tilde{u}_{nk})}{\partial\tilde{t}} + \frac{u_{n0}}{\nu_nL} \tilde{n}_n\tilde{u}_{nj} \frac{\partial\tilde{u}_{nk}}{\partial\tilde{x}_j} \right. \\ \left. + \frac{k_bT_{n0}}{m_n\nu_nu_{n0}L} \tilde{T}_n \frac{\partial\tilde{n}_n}{\partial\tilde{x}_k} + \frac{\mu_n}{n_{n0}m_n\nu_nL^2} \frac{\partial^2\tilde{u}_{nk}}{\partial\tilde{x}_j\partial\tilde{x}_j} + \tilde{n}_n\tilde{u}_{nk} \right) = 0, \end{aligned} \quad (15)$$

where $\mathcal{O}(\frac{1}{t_0\nu_n}) \sim \mathcal{O}(1)$, $\mathcal{O}(\frac{u_{n0}}{\nu_nL}) \sim \mathcal{O}(10^{-9})$, $\mathcal{O}(\frac{k_bT_{n0}}{m_n\nu_nu_{n0}L}) \sim \mathcal{O}(1)$, and $\mathcal{O}(\frac{\mu_n}{n_{n0}m_n\nu_nL^2}) \sim \mathcal{O}(1)$, respectively. Since $\mathcal{O}(\frac{n_{n0}m_n\nu_{n0}u_{n0}}{n_{e0}m_e\nu_{e0}u_{e0}}) \sim \mathcal{O}(10^{-3}) \sim \mathcal{O}(\epsilon_e)$, we acquire

$$\mathcal{O}(\epsilon_e) : \frac{\partial(\tilde{n}_n\tilde{u}_{nk})}{\partial\tilde{t}} + \tilde{T}_n \frac{\partial\tilde{n}_n}{\partial\tilde{x}_k} + \frac{\partial^2\tilde{u}_{nk}}{\partial\tilde{x}_j\partial\tilde{x}_j} + \tilde{n}_n\tilde{u}_{nk} = 0. \quad (16)$$

For the steady state, equation (16) means the driving force for the neutral radical is the density gradient $\tilde{T}_n \frac{\partial\tilde{n}_n}{\partial\tilde{x}_k}$, which is balanced by the collision term $\tilde{n}_n\tilde{u}_{nk}$ and viscous term $\frac{\partial^2\tilde{u}_{nk}}{\partial\tilde{x}_j\partial\tilde{x}_j}$.

Table 2. Estimation of the magnitudes of characteristic quantities.

Parameter	Unit	Characteristic	Magnitude	Comment
T_e	K	T_{e0}	$\sim 10^4$	Electron temperature measured in experiment, magnitude in 1 eV (Narishige <i>et al</i> 2000, Yamada <i>et al</i> 2007).
u_e	m s^{-1}	u_{e0}	$\sim 10^{5.5}$	Estimated as $k_b T_{e0}/2 = m_e u_{e0}^2/2$.
n_e	m^{-3}	n_{e0}	$\sim 10^{17}$	Experimental value range from (Grotjohn <i>et al</i> 2000, Narishige <i>et al</i> 2000, Derkaoui <i>et al</i> 2014). Affected by microwave power and gas pressure.
ν_e	s^{-1}	/	$\sim 10^{10}$	Theoretical calculated value from (Hassouni <i>et al</i> 2010) when electron energy is 1 eV and total gas density is 10^{24} m^{-3} .
E_k	$\text{V} \cdot \text{m}^{-1}$	E_{k0}	$\sim 10^5$	Numerical value by solving the Maxwell's equations from (Wang <i>et al</i> 2020) and our own result in figure 4.
T_i	K	T_{i0}	$\sim 10^3$	Experimental and numerical value from (Gicquel <i>et al</i> 1994, 1996, Hassouni <i>et al</i> 1999a, 2010)
u_i	m s^{-1}	u_{i0}	$\sim 10^{-1}$	Estimated by the inlet rate ~ 100 SCCM through a pipeline with diameter of 3 mm
n_i	m^{-3}	n_{i0}	$\sim 10^{17}$	Assumed to be the same as n_{e0} .
ν_i	s^{-1}	/	$\sim 10^{10}$	Assumed to be the same as ν_{e0} .
T_n	K	T_{n0}	$\sim 10^3$	Assumed to be the same as T_{i0} .
u_n	m s^{-1}	u_{n0}	$\sim 10^{-1}$	Estimated by the inlet rate ~ 100 SCCM through a pipeline with diameter of 3 mm
n_n	m^{-3}	n_{n0}	$\sim 10^{20}$	Value taken from (Hassouni <i>et al</i> 1999b, 2010) when electron energy is 1 eV and total gas density is 10^{24} m^{-3} .
ν_n	s^{-1}	/	$\sim 10^8$	Estimated by $n_t \sigma_t \nu_{\text{th}}$, where n_t is total gas number density 10^{24} m^{-3} , σ_t is total collision cross-section 10^{-19} m^2 , and ν_{th} is thermal velocity of gas 10^3 ms^{-1} .
μ_n	$\text{Pa} \cdot \text{s}$	μ_{n0}	$\sim 10^{-5}$	Theoretical calculated value from (Boulos <i>et al</i> 2023).
t	s	t_0	$\sim 10^{-10}$	Estimated as the reciprocal of ν_{e0} .
x	m	L	$\sim 10^{-2}$	Dimension of the resonant chamber.

Returning to the dimensional form, for the steady state, equations (12), (14), and (16) are on the same order of magnitude and their expressions are

$$n_e m_e u_{ej} \frac{\partial u_{ek}}{\partial x_j} + k_b T_e \frac{\partial n_e}{\partial x_k} = 0, \quad (17)$$

$$k_b T_i \frac{\partial n_i}{\partial x_k} + n_i m_i \nu_i u_{ik} = 0, \quad (18)$$

$$k_b T_n \frac{\partial n_n}{\partial x_k} + \mu_n \frac{\partial^2 u_{nk}}{\partial x_j \partial x_j} + n_n m_n \nu_n u_{nk} = 0. \quad (19)$$

The steady-state continuity equations for the electron, ion and neutral radical are listed as

$$\frac{\partial (n_e u_{ek})}{\partial x_k} = S_e, \quad (20)$$

$$\frac{\partial (n_i u_{ik})}{\partial x_k} = S_i, \quad (21)$$

$$\frac{\partial (n_n u_{nk})}{\partial x_k} = S_n, \quad (22)$$

where S_e, S_i, S_n are the source terms for the electron, ion, and neutral radical, and they can generally assumed to be related

to the electron number density, respectively. We take S_e as an example. It is a balance between two parts: the generation term G_e and the loss term L_e by collision processes (Lieberman and Lichtenberg 1994). G_e stands for a physical process such that an electron collides with a neutral molecule or a charged ion to produce a secondary electron. It is subsequently proportional to the electron number density and electron energy, where the electron energy is gained from the electric field and should be proportional to the electric magnitude squared. Therefore, the generation term is expressed as $G_e = R_i E^2 n_e$, where R_i is generally called the ionization coefficient. On the other hand, the loss term means an electron collides with a charged ion and forms a new neutral molecule or a new charged ion, which is called a recombination process. That is to say that L_e is proportional to the electron number density times the ion number density, and can be expressed as $L_e = R_{vr} n_e n_i = R_{vr} n_e^2$, where R_{vr} is the recombination coefficient and $n_e = n_i$ for charge balance. That means $S_e = G_e - L_e = R_i E^2 n_e - R_{vr} n_e^2$. Similarly, the source term for ions is $S_i = G_i - L_i = R_i E^2 n_e - R_{vr} n_e^2$. It is reasonable to assume that the neutral radical generation and loss are proportional to S_e . For simplicity, we assume $S_n = S_e = R_i E^2 n_i - R_{vr} n_i^2$ for the proportionality factor being one.

2.3. Simplified governing equations

Combining equations (17) and (20), the governing equation for the electron number density can be given in a common Poisson equation form as

$$\frac{\partial}{\partial x_k} \left(-D_e \frac{\partial n_e}{\partial x_k} \right) = R_i E^2 n_e - R_{vr} n_e^2, \quad (23)$$

where $D_e = \frac{k_b T_e}{m_e u_{ek} \frac{\partial u_{ek}}{\partial x_j}}$ is defined as the diffusion coefficient of the electron. Similarly, we can combine equation (18) with (21) and obtain

$$\frac{\partial}{\partial x_k} \left(-D_i \frac{\partial n_i}{\partial x_k} \right) = R_i E^2 n_e - R_{vr} n_e^2, \quad (24)$$

where $D_i = \frac{k_b T_i}{m_i \nu_i}$ is the diffusion coefficient of the ion. Considering the ambipolar diffusion to keep the quasi-neutrality of the plasma, the ambipolar diffusion coefficient $D_a = D_i \left(1 + \frac{T_e}{T_i} \right)$ is adopted to substitute D_e, D_i in equations (23) and (24):

$$\frac{\partial}{\partial x_k} \left(-D_a \frac{\partial n_e}{\partial x_k} \right) = R_i E^2 n_e - R_{vr} n_e^2 \quad (25)$$

$$\frac{\partial}{\partial x_k} \left(-D_a \frac{\partial n_i}{\partial x_k} \right) = R_i E^2 n_e - R_{vr} n_e^2. \quad (26)$$

In this way, the ion distribution is the same as the electron, which guarantees the quasi-neutrality of the plasma and spares the effort of solving the Poisson equation. Combining equations (19) and (22), we acquire

$$\frac{\partial}{\partial x_k} \left(-D_n \frac{\partial n_n}{\partial x_k} - \gamma_n \frac{\partial^2 u_{nk}}{\partial x_j \partial x_j} \right) = R_i E^2 n_e - R_{vr} n_e^2, \quad (27)$$

where $D_n = \frac{k_b T_n}{m_n \nu_n}$ is the diffusion coefficient of the neutral radical. $\gamma_n = \frac{\mu_n}{m_n \nu_n}$ has a unit of m^{-1} , which means the number of collisions per meter, and depicts the intensity of the viscous dissipation in space. It is worth mentioning that the above diffusion coefficient should be effective because of the nature of the multi-component mixture. We note that the expressions for D_a and D_n contain the corresponding collision frequencies, which are mostly determined by the collision with the gas mixture since the gas mixture has the largest number density, as shown in table 1. Therefore, the above diffusion coefficients are chosen based on the number density of the gas mixture.

The corresponding boundary conditions for equations (25), (27), (7), and (8) are

$$n_e|_{\text{wall}} = 0, \quad (28)$$

$$n_n|_{\text{wall}} = 0, \quad (29)$$

$$u_g|_{\text{wall}} = 0, \quad (30)$$

$$u_g|_{\text{inlet}} = u_{\text{in}}, \quad (31)$$

$$p|_{\text{outlet}} = P_g, \quad (32)$$

where u_{in} is the inlet velocity of the neutral gas, and P_g is the chamber pressure, where equation (32) means the outlet flow is fully developed. The velocity of the neutral radical u_n is regarded as the same as the gas mixture velocity u_g because the neutral radical has no charge and is not influenced by the electric field. The boundary conditions, equations (28) and (29), are chosen because the MPCVD equipment is linked with the ground and all the electrons are directed away to the ground very quickly. In addition to these equations, the electric field is obtained by numerically solving Maxwell's equations.

In the present work, we do not consider the heterogeneous surface reactions occurring in the diamond surfaces. This means that the solid boundary in the diamond is spatially constant. In actual physical processes, especially in the case of diamond deposition, competitive growth of graphite and diamond occurs at the surface, and etching processes including H atoms are necessary to suppress the graphite phase and allow the diamond phase to grow during the deposition process.

3. Results and discussion

3.1. Solvers and geometry

To properly solve the above equations, we adopt COMSOL 6.1, a widely accepted finite element method (FEM) solver for multi-physics problems. The Maxwell equations are combined and expressed in frequency form:

$$\nabla \times \left[\mu_{em}^{-1} (\nabla \times \tilde{\vec{E}}) \right] + \left[jw \frac{e^2 n_e}{m_e (\nu_e + jw)} - w^2 \epsilon_{em} \right] \tilde{\vec{E}} = 0, \quad (33)$$

where w is the microwave frequency, μ_{em} is the relative magnetic permeability of plasma, ϵ_{em} is the relative electric permittivity of plasma, and j is the imagination unit. $\tilde{\vec{E}}$ is the time-independent electric field magnitude. Here, the plasma is equivalent to a dielectric, whose electric conductivity is related to the electron number density, and is expressed as $\sigma_{em,p} = \frac{e^2 n_e \nu_e}{m_e (\nu_e^2 + w^2)}$ (Hagelaar *et al* 2004). The boundary condition for equation (33) is the perfect electric conductor. The microwave energy is imported by the S-parameter calculation numerically. The governing equations for the electron and neutral radical number density, equations (25) and (27), are implemented by the coefficient form PDE interface in the mathematics module. The governing equations for the neutral gas flow, equations (7) and (8), are solved by the laminar flow module.

The geometry that we simulate is shown in figure 1, which is an efficient and compact CVD system in actual production. The microwave is imported from the downside. Passing in order a waveguide, BJ26, an antenna, and a quartz glass, the microwave is directed into the gas chamber, where the gas mixture, mainly H_2/CH_4 , enters from the upside through four gas inlets. The diamond seed crystal is placed onto a molybdenum plate. The molybdenum plate is cylindrical with a diameter of 80 mm and a height of 8 mm. Previous research

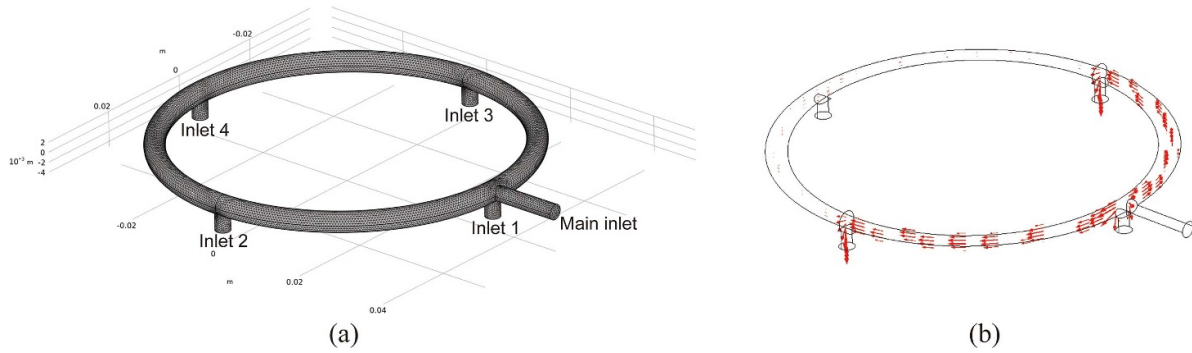


Figure 2. (a) Gas inlet apparatus with grids for inlet velocity determination. One single main inlet bifurcates into four inlets after an annulus, and therefore the four inlet velocities differentiate from each other. (b) Velocity vector plot to demonstrate the velocity distribution.

Table 3. Inlet velocity results for the following case setup.

	Case 1	Case 2	Case 3	Case 4
Main inlet (m s^{-1})	0.11	0.18	0.27	0.36
Inlet 1 (m s^{-1})	0.06	0.12	0.19	0.25
Inlets 2 and 3 (m s^{-1})	0.01	0.02	0.03	0.05
Inlet 4 (m s^{-1})	0.003	0.01	0.01	0.02

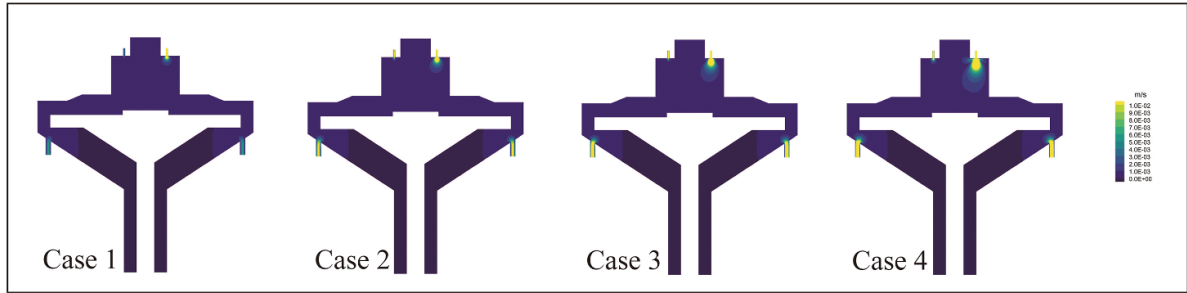
(Cuenca *et al* 2022) has demonstrated that this molybdenum plate has little effect on the resonant frequency of the whole chamber. In our study, the Poisson-type equation and the Navier–Stokes equations are solved in a coupled manner, which generally require high-quality mesh for numerical convergence and are out of the capability of unstructured grids. Therefore, the structured grids are chosen for the present study and obtained in high quality using ICEM software, as shown in figures 1(c) and (d). A high-performance computer is adopted for simulation due to its large computation cost, with 64 cores in 2.0 GHz and 512 GB total memory. The typical simulation time is several hours for a single case in our present work.

3.2. Validation

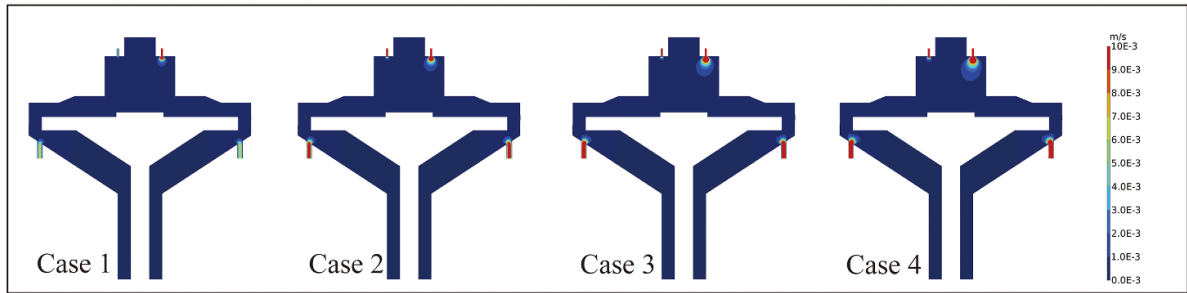
First, the validation of the flow simulation and grid-independence test are presented. There are four neutral gas inlets in our simulation domain, which are noted as inlets 1, 2, 3, 4 as figure 2 shows, and which have different velocity. In the actual experiment, the gases H_2 and CH_4 are pre-mixed and then injected through a single pipeline, which is the main inlet shown in figure 2(a) and has a diameter of 3 mm. After the main inlet, the gas is directed into a circulation loop and subsequently enters the gas chamber through the four inlets, which are inlets 1, 2, 3, 4 with diameter 3 mm and use the same notation as in figure 1. This apparatus is simulated to obtain the different velocities for the four inlets, where the boundary conditions are set such that the main inlet is the velocity inlet and the inlets 1, 2, 3, 4 are pressure outlets. We consider four cases, in which the main inlet velocity is set as 0.11 m s^{-1} , 0.18 m s^{-1} , 0.27 m s^{-1} , and 0.36 m s^{-1} respectively, and the four inlet velocity results are shown in table 3. The results demonstrate

that the velocities of the four separate inlets have large differences due to the annulus inlet design, and these results are used for the subsequent simulation of flow in the chamber.

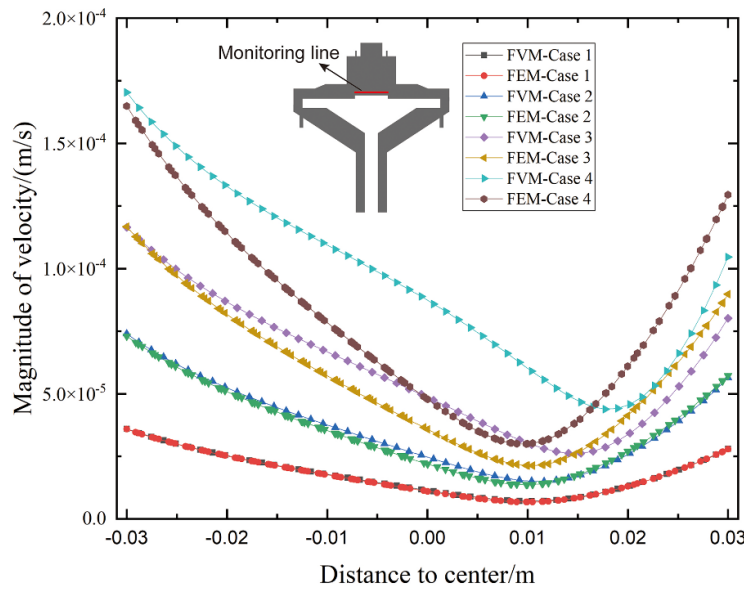
The flow field results obtained by FEM for the four different cases, defined in table 3, are compared with ANSYS Fluent, a finite volume method (FVM) solver, which is generally believed to be the most accurate for fluid flow simulation and adopted as the benchmark for our FEM flow simulation. For FEM and FVM, a grid-independence test is conducted. The same structured mesh shown in figure 1 is used and we change the number of the grids to 320 744, 444 400, 577 016, and 738 528, respectively. The simulation results show that there is no change in the flow fields after the mesh number is larger than 577 016 for both FEM and FVM. As a result, all subsequent simulations adopt the grid number as 577 016. The comparison of velocity contours between FVM and FEM is demonstrated in figure 3. The velocity contours are plotted in the same colormap range and the FVM and FEM results for the corresponding cases depict almost the same velocity field. For a detailed comparison, the velocity magnitudes are plotted on a monitoring line, which is 3 mm above the molybdenum plate and is symmetric about the central axis of the apparatus with 60 mm in length, as shown in figure 3. We demonstrate that the FEM results for low velocity in cases 1 and 2 are consistent with the FVM results and deviate with the increase in inlet velocity, while they can still capture the flow profile with reasonable tolerance for cases 3 and 4. Typically, FVM has higher accuracy. These comparisons show that FEM can accurately obtain the flow field for low inlet velocity, but it is not suitable for simulating higher velocity. For higher velocity, the quality of the mesh needs further improvement and the mesh number should increase, which may even require local



(a)



(b)



(c)

Figure 3. The flow fields for four different cases: (a) FVM results; (b) FEM results. (c) Comparison of magnitude of velocity between FVM and FEM for a monitoring line. The line is symmetric about the central axis of the apparatus, which is 3 mm above the molybdenum plate and 60 mm in length.

mesh refinement and will be beyond the computational capability after coupling other fields with the flow field. Due to this, for our present study, we do not calculate higher velocity except for the current four cases and adopt FEM for subsequent simulation since the FEM solver can handle multi-physics simulation.

After validation of the velocity calculation, multi-physics simulations are conducted. Solving equations (33), (25), (27), (7), and (8) together, the contours for electric field magnitude and electron number density, both in 3D multi-slice and 2D slice, are depicted in figure 4, and the corresponding parameter values are given in table 4. The electric field is

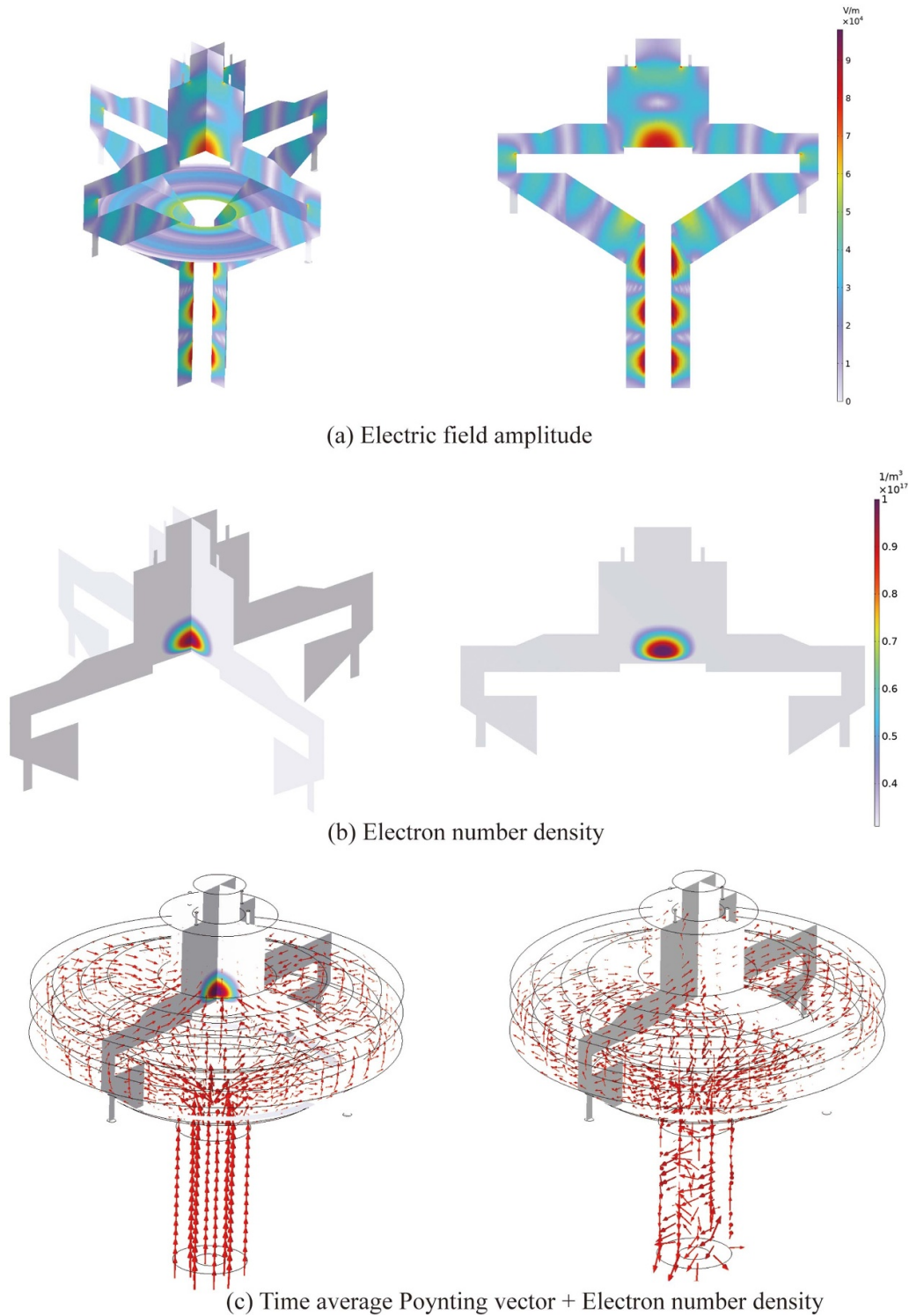


Figure 4. Simulation results. (a) The electric field amplitude in 3D multi-slice and 2D slice. (b) The electron number density. (c) Time-averaged Poynting vector (in arrow) + electron number density (in contours of multi-slice), with plasma (left) and without plasma (right).

concentrated above the molybdenum plate in the gas chamber and excites the plasma ball. The key value is the maximum of the electron number density, which can be quantitatively compared with experimental measurements. The different

experimental results, which are obtained by optical emission spectroscopy (OES) (Derkaoui *et al* 2014), millimeter-wave open resonator (Grotjohn *et al* 2000), and Thomson scattering measurement (Narishige *et al* 2000), consistently

Table 4. Values of parameters used in numerical simulation.

Parameter	Value	References
w	2.45 GHz	\
μ_{em}	0	\
ϵ_{em}	1	\
D_a	$0.2 \text{ m}^2\text{s}^{-1}$	Estimated value based on theoretical value from BOLSIG+ (Hagelaar and Pitchford 2005)
R_{vr}	$1 \times 10^{-13} \text{ m}^{-3}\text{s}^{-1}$	Estimated value based on experimental measurement in (Glosik <i>et al</i> 2003)
R_i	$2 \times 10^{-6} \text{ m}^{-3}\text{s}^{-1}$	Experimental measurement in (Derkaoui <i>et al</i> 2014)
P_{in}	5800 W	Experimental setup in (Wang <i>et al</i> 2020) for the same geometry
P_g	13000 Pa	Experimental setup in (Wang <i>et al</i> 2020) for the same geometry

demonstrate that the maximum of the electron number density is on the magnitude of 10^{17} m^{-3} . Our simulation result in figure 4(b) presents the maximum electron number density to be 10^{17} m^{-3} , which agrees with experimental measurements. It is worth mentioning that the corresponding value of the ionization coefficient, R_i , is also consistent with experimental observations (Derkaoui *et al* 2014). To further illustrate the effect of the plasma on the electric field, the time-averaged Poynting vector, which represents the electromagnetic energy flow, is plotted with and without plasma in figure 4(c). With plasma, the energy flows into the plasma in a highly orderly manner, while the energy flow has no single flow direction without the plasma.

3.3. Viscous effect

Finally, the neutral radical number density results are presented in figure 5. The parameters for neutral radical number density simulation are calibrated as $D_n = 0.17 \text{ m}^2\text{s}^{-1}$ and $\gamma_n = 5 \times 10^{17} \text{ m}^{-1}$. The contours of the neutral radical number density for the four cases in figure 5(a) clearly demonstrate non-uniformity with the increase in inlet velocity. For better illustration, the ratios between the electron and neutral radical number density on a monitoring line, which is 3 mm above the molybdenum plate with 40 mm in length and symmetric about the central axis of the apparatus, are plotted in figure 5(b). The results show that the maximum ratio rises from 1.5 for case 1 to about 3.6 for case 4. This proves that the non-uniformity of the neutral radical number density strengthens with the inlet velocity. The deposition rate mainly relies on the excited neutral radical and this non-uniformity therefore has a significant influence on the deposited crystal. For qualitative comparison, we plot the experiment results from the literature (Wang *et al* 2020) in figure 5(c). In the literature, they measure the intensity ratio between the atomic hydrogen line H_α at 656.5 nm and the C2 swan at 516.5 nm based on the OES measurement, and also the average growth rate of diamond. Generally, the

intensity of H_α is proportional to the electron density, and C2 is one of the most common neutral radicals in the plasma. In the simulation, the geometry and input parameters are the same as the ones in the experiment. Figure 5(c) demonstrates the same trend as in our simulations. Therefore, this consistency qualitatively validates our simulation results and theoretical analysis. Nonetheless, we do not plot our simulation results and the experimental results in the same figure because they only match with each other qualitatively. One possible reason for this may be that other neutral radicals except C2, like CH_x , can exist in the plasma phase. For quantitative comparison, we need to consider the complete plasma reactions and surface reactions in our future work.

Our findings provide a novel insight into how neutral radical spatial distribution is influenced by the neutral gas flow, and into the regulation of MPCVD and possibly other CVD methods. On the one hand, this phenomenon should be prohibited since it causes a non-uniform deposition rate and increases the risk of breakage. On the other hand, it also implies an approach for controlling the distributions of neutral radicals in the plasma and thus a novel mechanism for improving the size and quality of deposited diamonds. Previous studies have illustrated experimentally that the flow rate affects the deposition rate (Ralchenko *et al* 1999) and product properties (Woehrl and Buck 2011, Liu *et al* 2016, Fauzi *et al* 2018, Emelyanov *et al* 2022) without changing the gas inlet design. Moreover, recent experimental observations (Wang *et al* 2020, Teng *et al* 2023, Zhao *et al* 2023) have demonstrated that the deposition rate is accelerated by only designing the gas inlet. The gas outlet design can also affect the n-type-doped efficiency of diamond using MPCVD (Ohtani *et al* 2014). These experiments are inspiring but lack a physical explanation. Qualitatively, our simulation results adopt the same geometry as in Wang *et al* (2020) and exhibit the same trend compared with experimental measurements in the same study. Our present work offers a mechanistic interpretation of such phenomena.

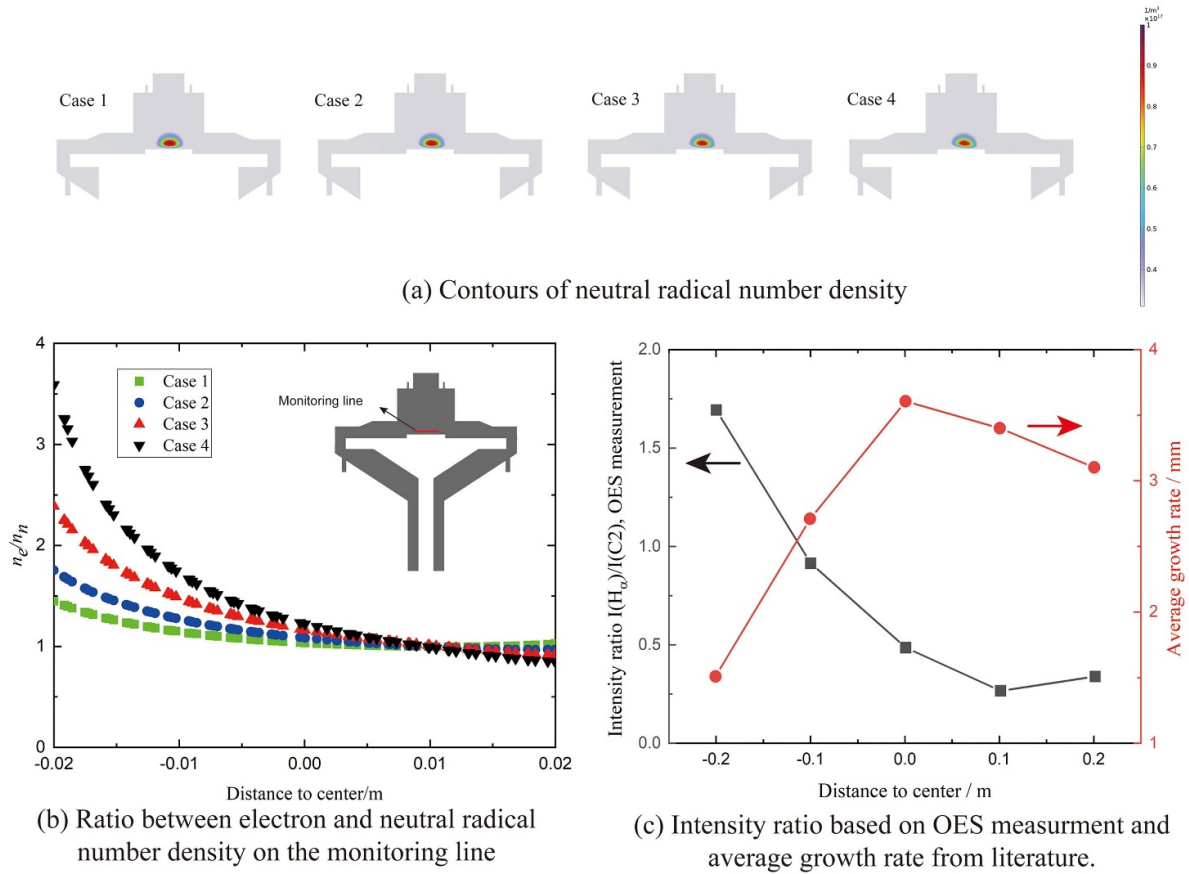


Figure 5. Simulation results and comparison with experimental measurement result from literature (Wang *et al* 2020). In the simulation, the geometry and input parameters are the same as those in the experiment. (a) Simulation results: contours of neutral radical number density; (b) Simulation results: the ratio between electron and neutral radical number density on the monitoring line, which is 3 mm above the molybdenum plate with 40 mm in length and symmetric about the central axis of the apparatus; (c) Experimental results (Wang *et al* 2020) in double-Y axis plot: the black line is the intensity ratio between the atomic hydrogen line H_{α} at 656.5 nm and the C2 swan at 516.5 nm based on OES measurement, and the red line is the average growth rate of diamond measured in actual production (Wang *et al* 2020). Generally, the intensity of H_{α} is proportional to the electron density and C2 is one of the common neutral radicals in the plasma.

4. Conclusion

In this work, we demonstrate that the spatial distribution of the neutral radical can be strongly affected by its viscous interaction with the neutral gas flow, and how an asymmetric inlet design can lead to non-uniformity of the neutral radical distribution. This mechanism is uncovered by deeply exploring the Boltzmann equation. By finding the momentum of the Boltzmann equation, the physical meaning of each term is clearly illustrated, by which the viscous term of the neutral radical is retained because the electron velocity is much higher than that of the neutral radical. After carefully analyzing the order of magnitude of different terms, simplified governing equations for the electron and neutral radical number density are obtained. It is worth noting that our derived electron number density equation has the same form as previous studies. Subsequently, solving the governing equations, including the Maxwell equations, the electron and neutral radical

number density equations, and the laminar Navier Stokes equations, validates our theoretical analysis, and this numerical tool provides a means for new apparatus design. Our simulation results are qualitatively consistent with the experimental results from the literature, and our findings indicate that the gas inlet design of the MPCVD equipment is an important factor to consider, which was generally overlooked in previous designs of MPCVD. Our present work is the first attempt, as far as we know, to simulate the MPCVD process in the 3D case, to demonstrate the importance of the flow field. To achieve the goal of 3D simulation, we introduce some assumptions and simplifications to make the computational cost affordable. Nonetheless, our result uncovers the mechanism of the flow field influence on the MPCVD and is instructive qualitatively because we point out that the flow field can be properly designed to optimize the MPCVD. Furthermore, this mechanism could probably be extended to explain the phenomena related to gas flow in other CVD methods quantitatively.

Data availability statement

No new data were created or analyzed in this study.

Acknowledgment

This work is financially supported by the NSF Grant of China (No. 12272207) and the Tsinghua University Initiative Scientific Research Program.

ORCID iD

Moran Wang  <https://orcid.org/0000-0002-0112-5150>

References

- Alves L L, Bogaerts A, Guerra V and Turner M M 2018 Foundations of modelling of nonequilibrium low-temperature plasmas *Plasma Sources Sci. Technol.* **27** 023002
- An K, Yu S W, Li X J, Shen Y Y, Zhou B, Zhang G J and Liu X P 2015 Microwave plasma reactor with conical-reflector for diamond deposition *Vacuum* **117** 112–20
- Ashfold M N R and Mankelevich Y A 2023 Two-dimensional modeling of diamond growth by microwave plasma activated chemical vapor deposition: effects of pressure, absorbed power and the beneficial role of nitrogen on diamond growth *Diam. Relat. Mater.* **137** 110097
- Ashfold M N and Mankelevich Y A 2022 Self-consistent modeling of microwave activated N₂/CH₄/H₂ (and N₂/H₂) plasmas relevant to diamond chemical vapor deposition *Plasma Sources Sci. Technol.* **31** 035005
- Bhatnagar P L, Gross E P and Krook M 1954 A model for collision processes in gases. I. Small amplitude processes in charged and neutral one-component systems *Phys. Rev.* **94** 511–25
- Boulos M I, Fauchais P L and Pfender E 2023 *Handbook of Thermal Plasmas* (Switzerland Springer)
- Bundy F, Hall H T, Strong H and Wentorfjun R 1955 Man-made diamonds *Nature* **176** 51–55
- Cuenca J A, Mandal S, Thomas E L and Williams O A 2022 Microwave plasma modelling in clamshell chemical vapour deposition diamond reactors *Diam. Relat. Mater.* **124** 108917
- Derkaoui N, Rond C, Gries T, Henrion G and Gicquel A 2014 Determining electron temperature and electron density in moderate pressure H₂/CH₄ microwave plasma *J. Phys. D: Appl. Phys.* **47** 205201
- Emelyanov A A, Pinaev V A, Plotnikov M Y, Rebrov A K, Timoshenko N I and Yudin I B 2022 Effect of methane flow rate on gas-jet MPCVD diamond synthesis *J. Appl. Phys.* **55** 205202
- Fauzi F B, Ismail E, Ani M H, Syed Abu Bakar S N, Mohamed M A, Majlis B Y, Md Din M F and Azam Mohd Abid M A 2018 A critical review of the effects of fluid dynamics on graphene growth in atmospheric pressure chemical vapor deposition *J. Mater. Res.* **33** 1088–108
- Füner M, Wild C and Koidl P 1995 Numerical simulations of microwave plasma reactors for diamond CVD *Surf. Coat. Technol.* **74** 221–6
- Füner M, Wild C and Koidl P 1999 Simulation and development of optimized microwave plasma reactors for diamond deposition *Surf. Coat. Technol.* **116–119** 853–62
- Gicquel A, Hassouni K, Breton Y, Chenevier M and Cubertafon J C 1996 Gas temperature measurements by laser spectroscopic techniques and by optical emission spectroscopy *Diam. Relat. Mater.* **5** 366–72
- Gicquel A, Hassouni K, Farhat S, Breton Y, Scott C D, Lefebvre M and Pealat M 1994 Spectroscopic analysis and chemical kinetics modeling of a diamond deposition plasma reactor *Diam. Relat. Mater.* **3** 581–6
- Glosik J, Novotný O, Pysanenko A, Zakouril P, Plašil R, Kudrna P and Poterya V 2003 The recombination of and ions with electrons in hydrogen plasma: dependence on temperature and on pressure of H₂ *Plasma Sources Sci. Technol.* **12** S117
- Gong Y et al 2024 Growth of diamond in liquid metal at 1 atm pressure *Nature* **629** 348–54
- Goodwin D G 1993b Scaling laws for diamond chemical-vapor deposition. I. Diamond surface chemistry *J. Appl. Phys.* **74** 6888–94
- Goodwin D 1993a Scaling laws for diamond chemical-vapor deposition. II. Atomic hydrogen transport *J. Appl. Phys.* **74** 6895–906
- Grotjohn T A, Asmussen J, Sivagnaname J, Story D, Vikharev A L, Gorbachev A and Kolysko A 2000 Electron density in moderate pressure diamond deposition discharges *Diam. Relat. Mater.* **9** 322–7
- Hagelaar G J M, Hassouni K and Gicquel A 2004 Interaction between the electromagnetic fields and the plasma in a microwave plasma reactor *J. Appl. Phys.* **96** 1819–28
- Hagelaar G J M and Pitchford L C 2005 Solving the Boltzmann equation to obtain electron transport coefficients and rate coefficients for fluid models *Plasma Sources Sci. Technol.* **14** 722–33
- Hassouni K, Gicquel A, Capitelli M and Loureiro J 1999a Chemical kinetics and energy transfer in moderate pressure H₂ plasmas used in diamond MPACVD processes *Plasma Sources Sci. Technol.* **8** 494
- Hassouni K, Grotjohn T and Gicquel A 1999b Self-consistent microwave field and plasma discharge simulations for a moderate pressure hydrogen discharge reactor *J. Appl. Phys.* **86** 134–51
- Hassouni K, Silva F and Gicquel A 2010 Modelling of diamond deposition microwave cavity generated plasmas *J. Phys. D: Appl. Phys.* **43** 153001
- Kamo M, Yurimoto H and Sato Y 1988 Epitaxial growth of diamond on diamond substrate by plasma assisted CVD *Appl. Surf. Sci.* **33** 553–60
- Kremer G M 2010 *An Introduction to the Boltzmann Equation and Transport Processes in Gases* (Springer Science & Business Media)
- Li X J, Tang W Z, Wang F Y, Li C M, Hei L F and Lu F X 2011 A compact ellipsoidal cavity type microwave plasma reactor for diamond film deposition *Diam. Relat. Mater.* **20** 374–9
- Li Y, Liu X, Shu G, Liu K, Zhao J, Zhang S, Yang L, Dai B, Zhu J and Han J 2020 Thinning strategy of substrates for diamond growth with reduced PCD rim: design and experiments *Diam. Relat. Mater.* **101** 107574
- Lieberman M A and Lichtenberg A J 1994 *Principles of Plasma Discharges and Materials Processing* (Wiley)
- Liu H, Zhu Y, Meng Q, Lu X, Kong S, Huang Z, Jiang P and Bao X 2016 Role of the carrier gas flow rate in monolayer MoS₂ growth by modified chemical vapor deposition *Nano Res.* **10** 643–51
- Loureiro J and Amorim J 2016 *Kinetics and Spectroscopy of Low Temperature Plasmas* (Springer)
- Mankelevich Y A, Ashfold M N and Ma J 2008 Plasma-chemical processes in microwave plasma-enhanced chemical vapor deposition reactors operating with C/H/Ar gas mixtures *J. Appl. Phys.* **104** 113304
- Mesbahi A, Silva F, Farhat S, Hassouni K, Bonnin X and Gicquel A 2013 Hydrodynamics effects in high power density microwave plasma diamond growth reactors *J. Phys. D: Appl. Phys.* **46** 385502
- Narishige S, Suzuki S, Bowden M D, Uchino K, Muraoka K, Sakoda T and Park W Z 2000 Thomson scattering

- measurement of electron density and temperature of a microwave plasma produced in a hydrogen gas at a moderate pressure *Jpn. J. Appl. Phys.* **39** 6732
- Neves A and Nazaré M H 2001 *Properties, Growth and Applications of Diamond* (Institution of Electrical Engineers)
- Ohtani R, Yamamoto T, Janssens S D, Yamasaki S and Koizumi S 2014 Large improvement of phosphorus incorporation efficiency in n-type chemical vapor deposition of diamond *Appl. Phys. Lett.* **105** 232106
- Pleuler E, Wild C, Fünér M and Koidl P 2002 The CAP-reactor, a novel microwave CVD system for diamond deposition *Diam. Relat. Mater.* **11** 467–71
- Prasanna S, Michau A, Rond C, Hassouni K and Gicquel A 2017 Self-consistent simulation studies on effect of methane concentration on microwave assisted H₂-CH₄ plasma at low pressure *Plasma Sources Sci. Technol.* **26** 097001
- Prasanna S, Rond C, Michau A, Hassouni K and Gicquel A 2016 Effect of buoyancy on power deposition in microwave cavity hydrogen plasma source *Plasma Sources Sci. Technol.* **25** 045017
- Ralchenko V, Sychov I, Vlasov I, Vlasov A, Konov V, Khomich A and Voronina S 1999 Quality of diamond wafers grown by microwave plasma CVD: effects of gas flow rate *Diam. Relat. Mater.* **8** 189–93
- Schreck M, Gsell S, Brescia R and Fischer M 2017 Ion bombardment induced buried lateral growth: the key mechanism for the synthesis of single crystal diamond wafers *Sci. Rep.* **7** 44462
- Su J J, Li Y F, Li X L, Yao P L, Liu Y Q, Ding M H and Tang W Z 2014 A novel microwave plasma reactor with a unique structure for chemical vapor deposition of diamond films *Diam. Relat. Mater.* **42** 28–32
- Teng Y, Zhao W, Tang K, Yang K, Zhao G, Zhu S, Ye J and Gu S 2023 High efficiency of boron doping and fast growth realized with a novel gas inlet structure in diamond microwave plasma chemical vapor deposition system *Carbon Lett.* **34** 1115–28
- Vikharev A L, Gorbachev A M, Lobaev M A and Radishev D B 2018 Multimode cavity type MPACVD reactor for large area diamond film deposition *Diam. Relat. Mater.* **83** 8–14
- Wang B, Weng J, Wang Z T, Wang J H, Liu F and Xiong L W 2020 Investigation on the influence of the gas flow mode around substrate on the deposition of diamond films in an overmoded MPCVD reactor chamber *Vacuum* **182** 109659
- Wang Q, Wu G, Liu S, Gan Z, Yang B and Pan J 2019 Simulation-based development of a new cylindrical-cavity microwave-plasma reactor for diamond-film synthesis *Crystals* **9** 320
- Woehrl N and Buck V 2011 Process control of CVD deposition of nanocrystalline diamond films by plasma diagnostics *Z. Phys. Chem.* **225** 1379–91
- Yamada H, Chayahara A and Mokuno Y 2007 Simplified description of microwave plasma discharge for chemical vapor deposition of diamond *J. Appl. Phys.* **101** 063302
- Yamada H, Chayahara A, Mokuno Y and Shikata S-I 2011 Model of reactive microwave plasma discharge for growth of single-crystal diamond *Jpn. J. Appl. Phys.* **50** 01AB02
- Yamada H, Chayahara A, Mokuno Y and Shikata S 2015 Numerical microwave plasma discharge study for the growth of large single-crystal diamond *Diam. Relat. Mater.* **54** 9–14
- Zhai Z, Zhang C, Chen B, Xiong Y, Liang Y, Liu L, Yang B, Yang N, Jiang X and Huang N 2024 Covalently-bonded diaphite nanoplatelet with engineered electronic properties of diamond *Adv. Funct. Mater.* **2401949**
- Zhao W et al 2023 An innovative gas inlet design in a microwave plasma chemical vapor deposition chamber for high-quality, high-speed, and high-efficiency diamond growth *J. Appl. Phys.* **56** 375104